

# Communication

## Influence of Grain-Refiner Addition on the Morphology of Fe-Bearing Intermetallics in a Semi-Solid Processed Al-Mg-Si Alloy

TAHSINA SMITH, KEYNA O'REILLY, SUNDARAM KUMAR, and IAN STONE

The three-dimensional morphologies of the Fe-bearing intermetallics in a semisolid-processed Al-Mg-Si alloy were examined after extracting the intermetallics.  $\alpha_c$ -AlFeSi and  $\beta$ -AlFeSi are the major Fe-bearing intermetallics. Addition of Al-Ti-B grain refiner typically promotes  $\beta$ -AlFeSi formation.  $\beta$ -AlFeSi was observed with a flat, plate-like morphology with angular edges in the alloy with and without grain refiner, whereas  $\alpha_c$ -AlFeSi was observed as “flower”-like morphology in the alloy with grain refiner.

DOI: 10.1007/s11661-013-1934-1

© The Minerals, Metals & Materials Society and ASM International 2013

Al-Mg-Si (6xxx) alloys are widely used heat-treatable alloys with superior combination of strength, ductility, and corrosion resistance compared with other Al alloys. Recycling of Al alloys entrains impurities such as Fe and Si. Since these impurities have low solid solubility in Al, they form various insoluble secondary intermetallic phases on solidification.<sup>[1]</sup> The type, size, and shape of the intermetallics vary depending on the local chemical composition and solidification conditions. Frequently observed intermetallics in 6xxx series Al alloys are cubic  $\alpha$ -Al<sub>3</sub>Fe<sub>2</sub>Si (or  $\alpha_c$ -AlFeSi) phase and monoclinic  $\beta$ -Al<sub>5</sub>FeSi (or  $\beta$ -AlFeSi) phase.<sup>[2–6]</sup>  $\alpha_c$ -AlFeSi is frequently observed with a complex interconnected dendritic structure, or “Chinese script” morphology, but can also be present in a multifaceted plate-like structure with rounded edges.  $\beta$ -AlFeSi is observed as a multifaceted plate-like structure with very high angular edges and branches.<sup>[7–11]</sup> It has also been noted that the addition of grain refiner may promote the formation of  $\beta$ -AlFeSi.<sup>[12]</sup> Unfortunately, the  $\beta$ -AlFeSi is unfavorable for downstream processing.<sup>[11]</sup> Homogenizing for long periods

gradually breaks up and transforms the plate-like  $\beta$ -AlFeSi into small, rounder  $\alpha_c$ -AlFeSi particles.<sup>[13]</sup> However, the improvement in properties is counterbalanced by a steep increase in manufacturing costs. Therefore, new cost-effective casting processes need to be developed to tolerate high-impurity contents.

The “New Rheocasting” (NRC) process<sup>[14]</sup> is of particular interest in the field of semisolid processing due to the advantage of not needing to use a special precursor material. A semisolid slurry with globular microstructure can be obtained by subjecting the melt to controlled cooling, and can then be cast into the required shape.<sup>[15]</sup> The advantages of NRC process compared with conventional casting processes include significant reduction in casting defects (such as porosity), and lower operating temperatures,<sup>[16]</sup> besides being 20 pct cheaper to run compared with conventional thixocasting.<sup>[15]</sup>

It is believed that the intermetallic phase morphology is dependent on the primary  $\alpha$ -Al grain size.<sup>[17]</sup> Park *et al.*<sup>[18]</sup> indicated that a 7xxx Al alloy processed *via* the NRC process had a consistent primary  $\alpha$ -Al grain size, irrespective of whether the alloy contained grain refiner or not. Therefore, in the current study, an attempt has been made for the first time to understand the influence of Al-Ti-B grain refiner on the type and morphology of Fe-bearing intermetallic phases independent of primary  $\alpha$ -Al grain size using semisolid processing of a 6xxx series Al alloy.

The base alloy (BA) used in the current study had a nominal chemical composition of Al-0.3Fe-0.5Si-0.40Mg, all in wt pct. This alloy was prepared by melting together commercially pure Al (99.97 pct), Al-80Fe master alloy, Al-50Si master alloy, and pure Mg (99.9 wt pct) in appropriate proportions. The processing technique employed was developed in-house to replicate the properties of NRC-processed 6xxx series Al, but on a smaller scale. The alloy was melted in an electric resistance furnace using a boron nitride-coated clay graphite crucible. At 1003 K (730 °C), the liquid metal was poured into a preheated [473 K (200 °C)] steel enthalpy can, such as the one used in the NRC process and allowed to cool down to 908 K (635 °C) before quenching the slurry in water. The steel enthalpy can was 185 mm in height with internal radii of 35 and 30 mm at the top and bottom, respectively, and a wall thickness of ~2.5 mm. A K-type thermocouple was used to monitor the temperature of the liquid inside the steel can, and the thermocouple tip was kept at a height of 150 mm from the bottom of the steel enthalpy can and at a distance of ~7.5 mm from the can center. Based on MTDATA analysis, at 908 K (635 °C), the alloy is expected to be 90 vol pct solid. For grain-refiner experiments, 0.02 wt pct of Al-5Ti-1B master alloy was added to the liquid metal before pouring into the steel enthalpy can. The alloy with grain refiner is referred to as GR.

Each billet was vertically sectioned, and all subsequent analyses were carried out at a height of ~150 mm from the bottom. For grain size measurement, one half of the vertically sectioned sample was ground using SiC abrasive paper and macroetched with Tucker's reagent

TAHSINA SMITH, D.Phil. Student, KEYNA O'REILLY, Lecturer, and SUNDARAM KUMAR, Research Fellow, are with Department of Materials, The EPSRC Centre for Innovative Manufacturing in Liquid Metal Engineering, University of Oxford, 16 Parks Road, Oxford, OX1 3PH, U.K. Contact e-mail: tahsina.smith@yahoo.com IAN STONE, Lecturer, is with Brunel Centre for Advanced Solidification Technology (BCAST), The EPSRC Centre for Innovative Manufacturing in Liquid Metal Engineering, Brunel University, Uxbridge, Middlesex, UB8 3PH, U.K.

Manuscript submitted October 10, 2012.

Article published online August 21, 2013

(45 pct HCl, 15 pct HF, 15 pct HNO<sub>3</sub>, and 25 pct H<sub>2</sub>O) from 3 to 4 minutes, until the grain structure was revealed. For cell size measurement, the cross-sectional sample was mounted in bakelite, grounded, and then fine polished with colloidal silica. The grain size and cell size were measured on optical microscope images using the mean linear intercept method.

For two-dimensional (2D) intermetallic analyses, 20 × 20 mm-sized samples were taken from the center of the cross section. Then, the mounted and polished samples were examined using a JEOL 840A scanning electron microscope (SEM) equipped with energy dispersive X-ray spectroscopy (EDX). For three-dimensional (3D) analyses, the samples were also taken from close to the center of the cross section. The intermetallics were then extracted using a similar procedure to that used by Simensen *et al.*,<sup>[17]</sup> in which anhydrous butan-1-ol is used to dissolve the  $\alpha$ -Al, leaving behind the unaffected intermetallic particles of interest dispersed on a polytetrafluoroethylene (PTFE) filter membrane (47-mm diameter, pore size of 2  $\mu$ m). In order to have a clear indication of the intermetallic morphology, the filter was put into the SEM, and the extracted particles were systematically examined at every ~400  $\mu$ m in a grid-like fashion.

The extracted intermetallic particles were also analyzed using a Philips 1700 series X-ray diffractometer (XRD), with Cu-K $\alpha$  at 1.54 Å wavelength. In order to reduce the preferred orientation, the intermetallic particles were ground to a powder with an agate pestle and mortar, and then carefully spread across a thin silicone-grease layer on a glass slide. The phases present in each sample were identified by comparing them with the spectra obtained for  $\beta$ -AlFeSi from the JCPDS reference patterns from the International Centre for Diffraction Data, and a theoretical plot for nonequilibrium  $\alpha_c$ -AlFeSi (since no pattern for reference was provided in the database). This theoretical plot was calculated<sup>[18]</sup> according to Cooper's suggestion of the  $\alpha_c$ -AlFeSi crystal structure.<sup>[19]</sup> Previous studies conducted at Oxford<sup>[20]</sup> have generated a regression curve, based on pure  $\alpha_c$ -AlFeSi and  $\beta$ -AlFeSi phases mixed in known proportions of 10 to 90 pct, to calculate the relative weight fractions of the two phases from XRD spectra. Three characteristic peaks were selected for both  $\alpha_c$ -AlFeSi and  $\beta$ -AlFeSi phases, which were then used to calculate the average peak intensities of the nine  $\beta$ -AlFeSi:  $\alpha_c$ -AlFeSi ratios,  $R$ :

$$R = 1/9 \left[ \sum_{i,j=1-3} (I_{\beta i}/I_{\alpha j}) \right],$$

where  $I_{\beta}$  are the intensities of the selected characteristic peaks of the  $\beta$ -AlFeSi phase, which are at 17.03, 20.81, and 28.96 deg  $2\theta$ , and  $I_{\alpha}$  are the intensities of the selected characteristic peaks of the  $\alpha_c$ -AlFeSi phase, which are at 22.37, 26.53, and 36.44 deg  $2\theta$ . The regression curve was drawn by fitting these points.

Figure 1 shows the grain size distribution across the cross section from the center to the near surface of the sample. The grain size and the cell size of the BA sample

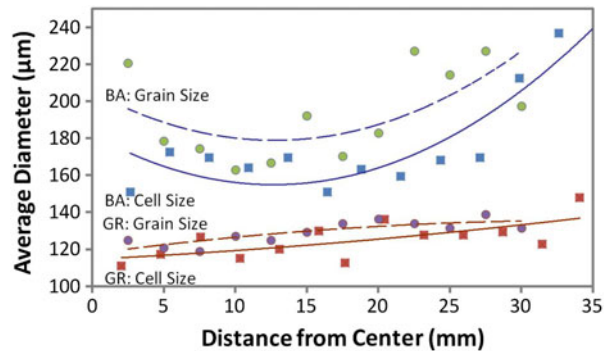


Fig. 1—The average primary  $\alpha$ -Al grain and cell size distribution from the center to the surface of the billets. The grain and cell sizes of the GR billet were small and both decreased uniformly from the surface.

decrease from the surface to about three-quarters of the way to the center, and then increase slightly toward the center. The addition of grain refiner reduces the grain size. The grain size and cell size of GR are more consistent from near the surface to the center than for the base alloy. Across the cross section, GR has a fine and uniform grain and cell size. It is interesting to note that the grain sizes of BA (163 to 227  $\mu$ m) observed in this investigation were significantly smaller than those observed in conventional casting methods (728 to 1309  $\mu$ m<sup>[21]</sup>). On the other hand, the GR grain sizes (119 to 138  $\mu$ m) matched very closely to the grain sizes of traditionally cast alloys with additions of Al-Ti-B grain refiners, which are typically in the range between 80 and 150  $\mu$ m.<sup>[22]</sup> This implies that the processing technique employed for this investigation was the dominant grain-size-determining factor for BA, where grain sizes comparable with 6xxx series Al alloys with additions of Al-Ti-B-type grain refiners could be produced.

The 2D analysis of the BA and GR samples show Fe-bearing intermetallics present at the cell/grain boundaries (Figures 2(a) and (b)). The higher magnification images (Figures 2(c) through (f)) show a combination of “needle”-like and “Chinese script”-like morphologies. It was interesting to note that most of the Fe-bearing intermetallics observed in BA had “needle”-like morphologies with a very few “Chinese script,” whereas, the GR microstructure contained a mixture of these two. In addition, the “Chinese script” intermetallics in BA were coarser and less intricate (Figure 2(c)) than in GR (Figure 2(d)). In GR, Ti-rich particles were also observed inside the primary  $\alpha$ -Al grains (Figure 2(d)), at a distance from the “Chinese script” intermetallics. The “needle”-like intermetallics in BA were noticeably longer and rougher (Figure 2(e)) than those in GR which appeared short and smooth (Figure 2(f)).

On extraction, it was evident that in 3D, the intermetallics in both samples were interconnected, with the filtrate appearing like black sponges in structure. On closer examination of the BA extracted sample (Figure 3(a)), a well-defined pore structure was evident. The diameters of the pores were measured to be 169

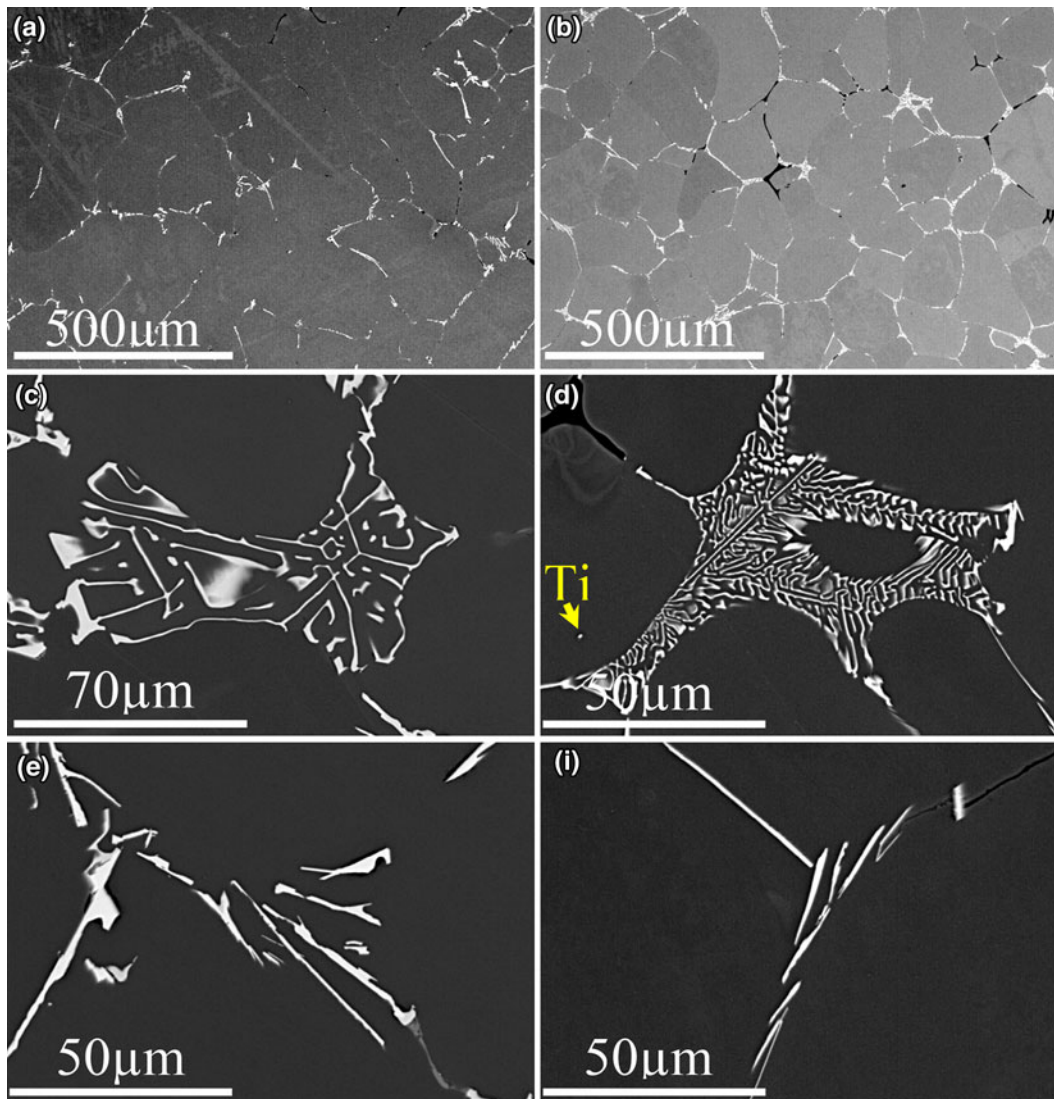


Fig. 2—BE-SEM images showing the 2D microstructure of (a, c, e) BA and (b, d, f) GR samples. “Chinese script” morphology of BA (c) is significantly larger and less intricate than that of GR (d). The “needle”-like intermetallics in BA (e) had a longer and rougher structure compared with GR (f).

( $\pm 15$ )  $\mu\text{m}$ , and the thicknesses of the intermetallics were  $< 1 \mu\text{m}$ . The surfaces of the 3D structures exhibit intricate patterns (Figures 3(c), (e), and (g)), some of which resembled (i) leaves, (ii) comb-like dendrites, (iii) multifaceted plates, and sometimes (iv) ripples, all curving around to create interconnected pores revealing where the primary  $\alpha\text{-Al}$  matrix had been. Based on their intricate morphology, these intermetallics were assumed to be  $\alpha\text{-AlFeSi}$  phase. Some phases were also observed that were flat with angular edges, and these multifaceted plates were assumed to be  $\beta\text{-AlFeSi}$  phase (Figure 3(e)).

The extracted samples from GR also exhibited well-defined pore structures (Figure 3(b)). The average diameter of the pores was measured to be  $132 \pm 15 \mu\text{m}$ . The surface exhibited patterns which resembled flowers with six “petals,” where each “petal” contained an angular feature at its tip (Figure 3(d)). The

average angles of the tips could be divided into two groups: one that averaged to  $\sim 120$  deg, and the second that averaged to  $\sim 90$  deg. However, no other characteristic features could be observed between the two groups of petals. Another common feature of the “petals” was that they had a skeletal morphology stretching from the centerline of each “petal” toward the edge, extending from the center of the “flower” up to the tips of the “petals.” Further investigation is required to locate the initiation point of the “flower”-like intermetallics. A second GR sample was prepared, and examined to locate Al-Ti-B phases. A few clusters of Ti-rich particles were observed to be scattered among the intermetallics (Figures 3(f) and (h)), but the distribution appeared to be rather random.

The 2D and 3D microstructures suggest that the cell size has a significant effect on the intermetallic phase morphology.<sup>[19,21,23,24]</sup> Although the surface features of

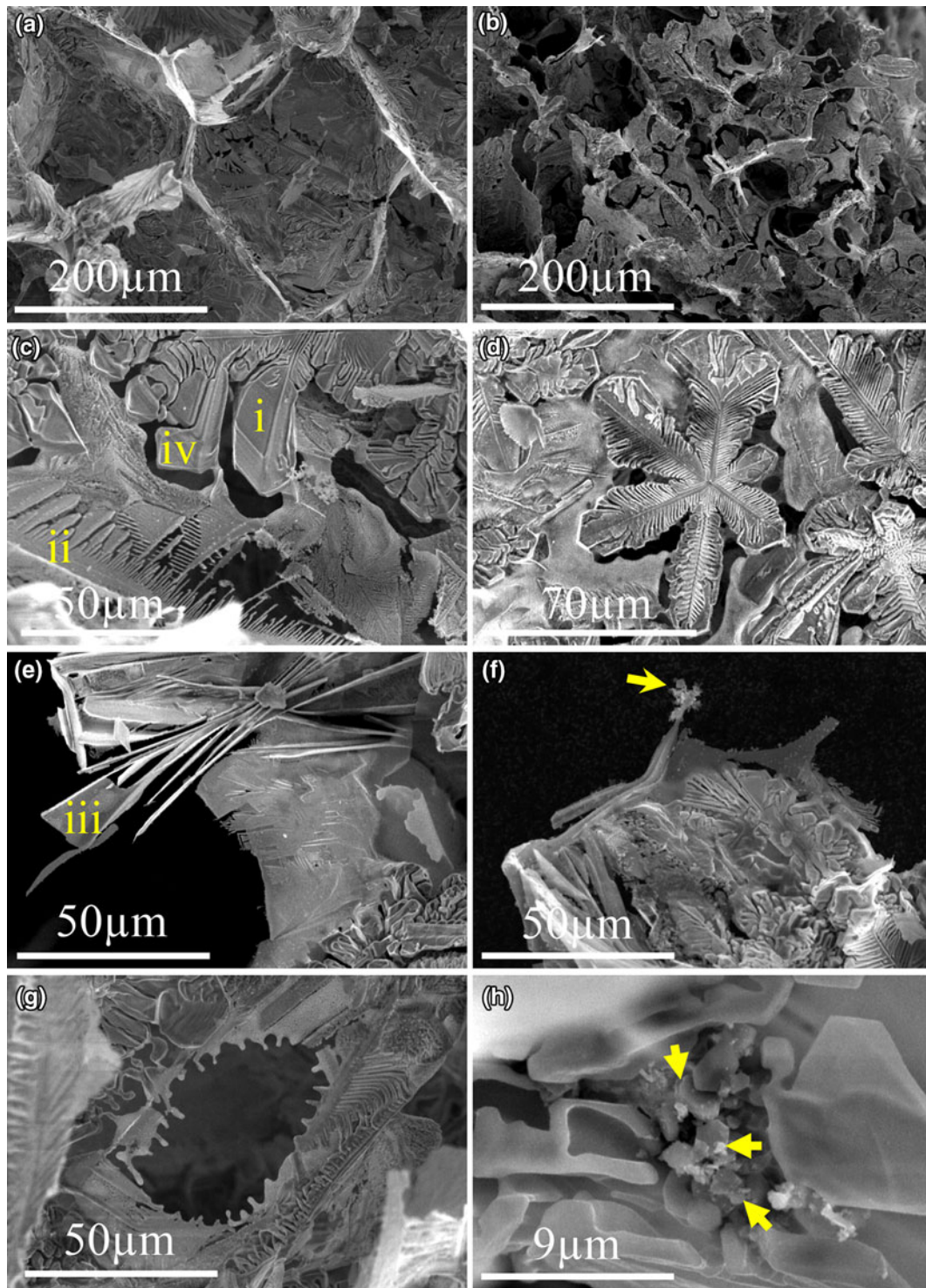


Fig. 3—SE-SEM images of the extracted intermetallics from the BA (a, c, e, g) and GR (b, d, f, h) billets. Arrows indicate Ti-rich particles. Different patterns that resemble (i) leaves, (ii) comb-like dendrites, (iii) multifaceted plates, and (iv) ripples have also been marked out.

the 2D particles appeared to be similar in detail, the 3D microstructure reveals that a smaller cell size leads to a much more compact and intricate intermetallic phase morphology. As cell size measurements from the 2D microstructure are comparable to the pore diameters (in 3D), it can be concluded that the intermetallic phase

encapsulate the aluminum cells, forming an interconnected fragile network. This phenomenon also implies that the intermetallic phases form after the  $\alpha$ -Al grains have initiated.

Figure 4 shows the XRD patterns from the extracted BA and GR samples. XRD results suggest that  $\alpha$ -AlFeSi

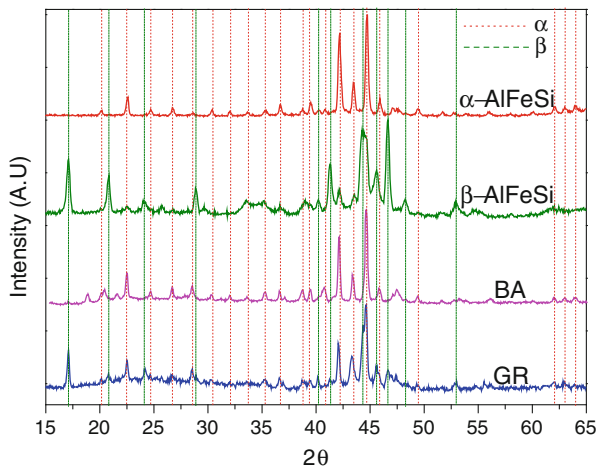


Fig. 4—XRD spectra of the extracted intermetallics from BA and GR billet.  $\alpha_c$ -AlFeSi is predominant in BA, whereas there was a more or less equal balance between  $\alpha_c$ -AlFeSi and  $\beta$ -AlFeSi in GR contents. Individual  $\alpha_c$ -AlFeSi and  $\beta$ -AlFeSi patterns are also plotted for reference.

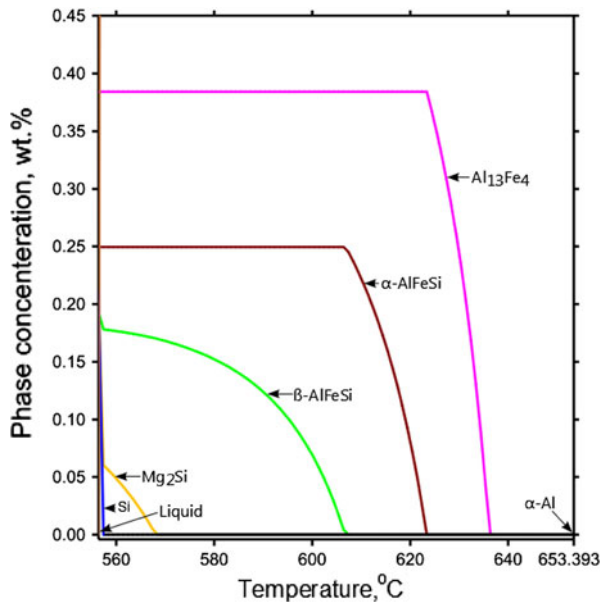


Fig. 5—Thermodynamic calculation of phase content, under Scheil condition.

and  $\beta$ -AlFeSi are the two major intermetallic phases observed in these alloys. Figure 5 shows the MTDATA simulation of the phases forming under partial-equilibrium Scheil solidification conditions for the studied BA alloy composition. It predicts the formation of  $\alpha$ -Al,  $\text{Al}_{13}\text{Fe}_4$ ,  $\alpha$ -AlFeSi,  $\beta$ -AlFeSi,  $\text{Mg}_2\text{Si}$ , and Si from the liquid. The absence of  $\text{Al}_{13}\text{Fe}_4$  in the XRD analysis in both the studied samples suggest that the solidification conditions in the NRC process either suppressed this solidification reaction kinetically such that no  $\text{Al}_{13}\text{Fe}_4$  was formed (or sufficient small quantity formed to be below the detection limit in XRD) or allowed for subsequent transformation to another phase through other invariant reactions.<sup>[25]</sup> The absence of  $\text{Mg}_2\text{Si}$  and

Si in the XRD pattern of this alloy billet is likely due to their contents being in low fractions below the detection limit of XRD. The XRD spectrum from BA indicated  $\alpha_c$ -AlFeSi as the predominant phase, and based on the relative peak intensities, it was calculated that, of the intermetallic present in BA,  $\sim 80$  wt pct was the proportion of  $\alpha_c$ -AlFeSi. For GR, the XRD spectrum indicated a greater proportion of the  $\beta$ -AlFeSi phase (more intense peak at 17.05 deg  $2\theta$ ), with wt pct of  $\alpha_c$ -AlFeSi being calculated to be  $\sim 60$  pct. Overall, the XRD analysis shows that  $\alpha_c$ -AlFeSi was predominant in both BA and GR, but that the proportion of  $\beta$ -AlFeSi was slightly higher in GR. Interestingly, based on the 2D microstructural analysis, BA appeared to have a much higher concentration of “needle”-like intermetallic in comparison with GR, where the “Chinese script”-like intermetallic was more prevalent. Thus, it can be concluded that assessment of phases and phase proportions cannot be reliably determined using 2D analysis.

The “needle”-like morphology that appears on the 2D microstructure can be attributed to the edges of the intermetallics or slices through intermetallic plates. Similarly, the “Chinese script” morphology which was predominantly observed at the triple-junctions of the boundaries may be a combination of  $\alpha$  and  $\beta$  as it displays part of the intricate patterns that lie underneath the  $\alpha$ -Al surface.

Figure 3(h) shows some of the titanium-rich particles that were observed in the 3D microstructure, and where they were positioned among the intermetallic particles. Based on Figure 3(f) it can be deduced that the Ti-rich particles can act as nucleating sites for the intermetallics, in particular encouraging the formation of  $\beta$ -AlFeSi phase due to a lower lattice misfit.<sup>[22]</sup> Figure 3(f) shows possible flat- and smooth-textured  $\beta$ -AlFeSi encapsulated by rippled and intricate  $\alpha_c$ -AlFeSi phase. This indicates the possibility that  $\alpha_c$ -AlFeSi phase is able to develop on top of a  $\beta$ -AlFeSi phase layer, which might explain the lack of traditional  $\beta$ -AlFeSi phase morphology among the extracted GR intermetallics.

Based on the observations of “flower”-shaped particles present within the extracted intermetallics and the Ti-rich particles studied, it may be assumed that the “flower”-like features in GR grow outward from the center. The six-“petal” shape at the center develops during nucleation by Ti-rich particles; each of those “petals” then follows a similar mechanism of intermetallic phase formation to that of BA. Figure 3(f) also indicates the possibility that the titanium-rich particle might have been a nucleating site for a “flower,” which may have broken off during sample preparation. The ridges on the “petals” could be due to the eutectic reaction between the  $\alpha$ -Al and the Fe-rich intermetallic phases. However, further investigation is required to test either theory. On the other hand, Figure 3(g) implies that when the intermetallics are not nucleated by Ti-rich particles, the intermetallics may grow inward and hence do not develop the six-“petal” shape.

Based on the findings presented, the following conclusions can be drawn from the current study. The intermetallics of the alloys produced for this investigation had high proportions of  $\alpha_c$ -AlFeSi phase. However, the

general trend still agreed with previous studies where the presence of Al-Ti-B-type grain refiner was found to promote  $\beta$ -AlFeSi phase formation. The “flower”-like morphology, which has not been observed previously, was possibly nucleated by potent substrates such as TiB<sub>2</sub>. The “non-six-petal flower”-like morphology, does not grow outward as it would appear in the grain-refined alloy. Instead, the net shape forms during initiation and develops into an intricate pattern as it solidifies.

---

## REFERENCES

1. I.J. Polmear: *Light Alloys: Metallurgy of the Light Metals*, 2nd ed., Edward Arnold, London, 1989.
2. S. Onurlu and A. Tekin: *J. Mater. Sci.*, 1994, vol. 29, pp. 1652–55.
3. G. Sha, K.A.Q. O’Reilly, B. Cantor, J. Worth, and R. Hamerton: *Mater. Sci. Eng. A*, 2001, vol. 304306, pp. 612–16.
4. N.C.W. Kuijpers, W.H. Kool, P.T.G. Koenis, K.E. Nilsen, I. Todd, and S. van der Zwaag: *Mater. Charact.*, 2003, vol. 49, pp. 409–20.
5. L. Sweet, S.M. Zhi, S.X. Gao, J.A. Taylor, and M.A. Easton: *Metall. Mater. Trans. A*, 2011, vol. 42A, pp. 1737–49.
6. S. Kumar, P.S. Grant, and K.A.Q. O’Reilly: *Trans. Indian Inst. Met.*, 2012, vol. 65, pp. 553–57.
7. L.F. Mondolfo: *Aluminum alloys, structure and properties*, Butterworths and Co. Ltd., London, 1976.
8. H. Ye: *J. Mater. Eng. Perform.*, 2003, vol. 12, pp. 288–97.
9. J.E. Eklund: Ph.D. Thesis, University of Technology, 1993.
10. J.A. Taylor, G.B. Schaffer, and D.H. St John: *Metall. Mater. Trans. A*, 1999, vol. 30A, pp. 1643–50.
11. J.L. Jorstad and W.M. Rasmussen: *Aluminum Casting Technology*, 2nd ed., Des Plaines, Illinois, USA, 2001, pp. 28–323.
12. I. Davidson: D.Phil. Thesis, University of Oxford, 2006.
13. S. Zajac, B. Hutchinson, A. Johansson, and L.O. Gullman: *Mater. Sci. Technol.*, 1994, vol. 10, pp. 323–33.
14. European Patent EP 0745694A1, UBE Industries Limited.
15. [http://www.metphys.mat.ethz.ch/research/new\\_rheo](http://www.metphys.mat.ethz.ch/research/new_rheo). Data Accessed on 24 April 2008.
16. *ASM Handbook, Volume 15: Casting*, ASM International, Metals Park, OH, 1998.
17. C.J. Simensen, P. Fartum, A. Andersen, and Z. Fresenius: *Anal. Chem.*, 1984, vol. 319, pp. 286–92.
18. S.B. Park, I.C. Stone, and B. Cantor: in *Rheocasting of Aluminium Alloys: Solidification of Aluminium Alloys*, M.G. Chu, D.A. Granger, and Q Han, eds., TMS, Warrendale, PA, 2004, pp. 257–66.
19. M. Cooper: *Acta Crystallogr.*, 1967, vol. 23, pp. 1106–07.
20. G. Sha: D.Phil. Thesis, University of Oxford, 2001.
21. A. Lui: D.Phil. Thesis, University of Oxford, 2010.
22. M. Jarrett, B. Neilson, and E. Manson-Whitton: in *Solidification and Casting*, B. Cantor, and K.A.Q. O’Reilly, eds., The Institute of Physics, Bristol, 2003, pp. 3–25.
23. S.B. Park: D.Phil. Thesis, University of Oxford, 2008.
24. A. Verma, S. Kumar, P.S. Grant, and K.A.Q. O’Reilly: *J. Alloys Compd.*, 2013, vol. 555, pp. 274–82.
25. G. Sha, K.A.Q. O’Reilly, B. Cantor, J.M. Titchmarsh, and R.G. Hamerton: *Acta Mater.*, 2003, vol. 51, pp. 1883–97.